more molecular, because the amorphous phases have lower densities which reduces the strengths of the back-bonds.

The pnictides have a variety of allotropic structures (fig. 11): rhombohedral (A7 or r-) As with three back-bonds, orthorhombic (o-) As with four back-bonds and the red phosphorus structure of P_4 molecules. The CRN describes the structure of annealed a-P, a-As and a-Sb quite well (fig. 11) [37, 150]. The covalent co-ordination is three and the average bond angle of a-As is 97°, with a broad dihedral angle distribution and rings of various order, as in a-Ge. The back-bonds are never explicitly included in the CRN building process and there are large 'caverns' in the network, the descendants of the interlayer spaces [38]. The layer correlations remain and perhaps produce a prepeak in the diffraction pattern [151–153]. These are not fully reproduced by the CRNs [38] possibly because the back-bonds are only given a minimum distance rather than an expectation value. Experimentally, r-As has a specific density of 5·72, while a-As can be sputtered with a density of 4·3–5·1 [38]. Thus, as the bond length remains unchanged at 2·49 Å, the density deficit must reflect larger back-bond distances.

The As co-ordination in r-As is distorted octahedral, related to the simple cubic lattice. The s^2p^3 valence configuration of As leaves non-bonding s electrons and one electron per p orbital. The p band is half-filled and metallic in the simple cubic structure but semimetallic when distorted [154, 155]. Our TB interactions [107] in table 1 used an sp^3 basis and were fitted to OPW and EPM calculations [156] and XPS data [157].

The valence DOS [157–159] of As shows the s states to be separated from the p states, unlike in Si. The s band DOS is twin-peaked for r-As but merges into a single peak in a-As (fig. 12), providing evidence of odd-membered rings [160]. The changes in the p bands are dominated by the opening of the optical gap in a-As of order 1·3 eV [38].

Fig. 11

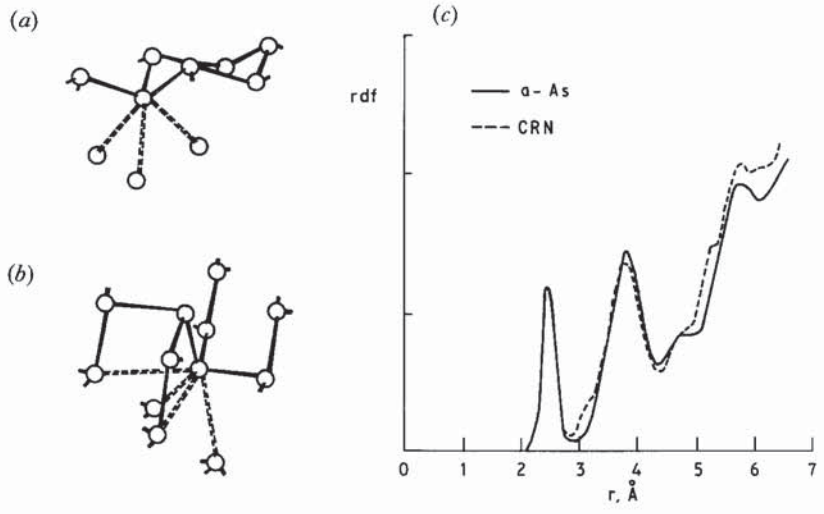

(*a*) Local order in rhombohedral As; (*b*) local order in orthorhombic As; (*c*) rdf in a-As.

Fig. 12

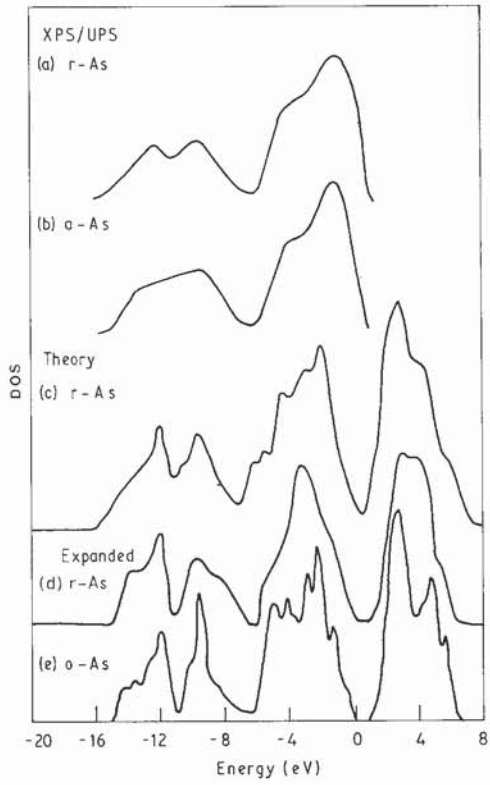

(*a*, *b*) Composite DOS of r-As and a-As, XPS [157] below −8 eV, UPS above −8 eV [159]. (*c*) TB DOS for r-As with normal 3·15 Å interlayer spacing, (*d*) expanded 3·85 Å spacing and (*e*) TB DOS of o-As. The calculations use the TB parameters of table 2 and emphasize the change in the σ–σ^* gap found in the earlier results of Kelly and Bullett [161, 162].

The opening of the optical gap in a-As is due to its weaker back-bonding. This can be seen schematically in the Peierl's-like model of Littlewood [154] or by direct band calculation. Figure 13 (*a*) shows the band structure of two r-As lattices, the first with the usual back-bond distance of 3·15 Å of r-As and the second for a distance of 3·85 Å, corresponding to a density of 5·1 of annealed a-As.

The influence of disorder on the *p*-like bands of a-As and a-Si is different because of arsenic's distorted octahedral co-ordination. In a-As (or a-Se) only the relative strength of front and back-bonds determines the optical gap, while angular distortions have little effect, unlike in a-Si. Angular changes alter the shape and peak heights within the σ and σ^* portions of the p bands rather than the positions of the band edges (fig. 12 (*b*)). This is confirmed by direct calculations on r-As and o-As [162]. Experimentally, the shape of the p DOS is a little unsettled [157–159].

The conduction bands of a-As have been probed by core spectroscopy [163]. The As 3*d* absorption spectrum (fig. 14) maps out the partial p DOS and shows the conduction band to be in two parts. The peak from 43–47 eV corresponds to the first 4*p* conduction band, while the second peak above 53 eV corresponds to a higher,

Fig. 13

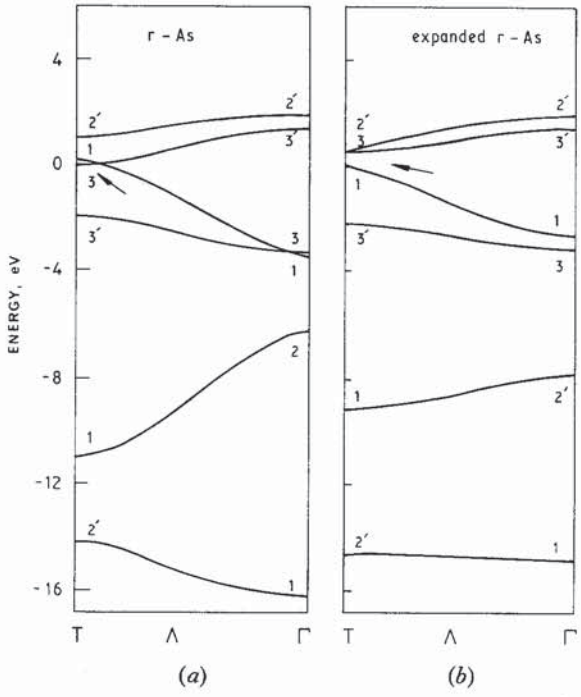

Calculated bands for r-As with (*a*) normal interlayer spacing of 3·15 Å and (*b*) expanded interlayer spacing of 3·85 Å. The opening of the gap at ε_f is arrowed.

Fig. 14

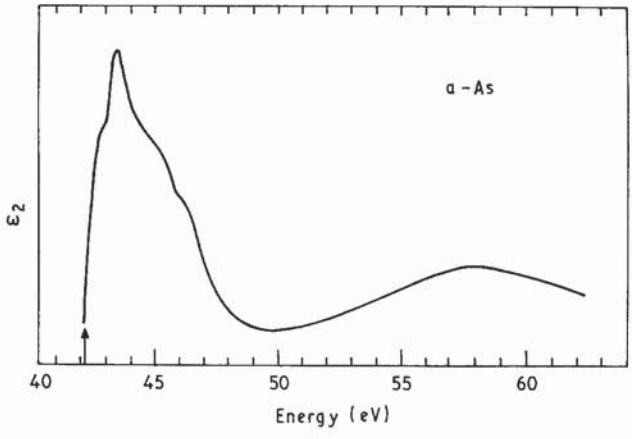

Core reflectivity spectrum of the 3*d* level in a-As, showing the first and second conduction band, after [163]. The arrow indicates the onset of core to band transitions, estimated from the core level energy from photoemission.

free-electron-like conduction band. The sharp feature at 42 eV is a core exciton and is resonant because it lies above the threshold for transitions to the conduction band, arrowed in fig. 14. The split conduction band of As contrasts sharply with the featureless conduction band of a-Si and is typical of lower co-ordinations such as Se.

The ε_2 optical spectra of r-As and a-As are compared in fig. 15. The spectrum of a-As shows a single broad peak at 3·5 eV, reminiscent of a-Ge [164], in spite of the split conduction bands, implying that most transitions terminate in the lower conduction band.

The principal properties of P have only recently been studied thoroughly [165–177]. P has a number of different allotropes. Crystalline black P has the layered orthorhombic structure to which it gives its name [166, 167]. Crystalline white P is a wide gap semiconductor containing P_4 molecules arranged in a large cubic unit cell. There is also a complicated crystalline form known as Hittorf's phosphorus containing columns of six-fold rings with other P atoms attached to form pentagonal tubes with five-fold rings of bonds [165]. There are few inter-column cross links. Amorphous (red) P is related to a-As but residual molecular effects may be more pronounced in a-P than in a-As and the uniform CRN is a poorer model for a-P. Finally, a-P : H can be deposited by a glow discharge in PH_3 [169, 170]. As P is lighter than As, we expect it to be more molecular, with relatively short intramolecular bonds and long intermolecular bonds. In fact the intermolecular bonds of P are close to the van der Waals limit indicating only small secondary bonding.

Pseudopotential and TB band calculations of o-P find a general band ordering similar to As [167–169]. The lowest valence states are *s*-like and the gap lies between

Fig. 15

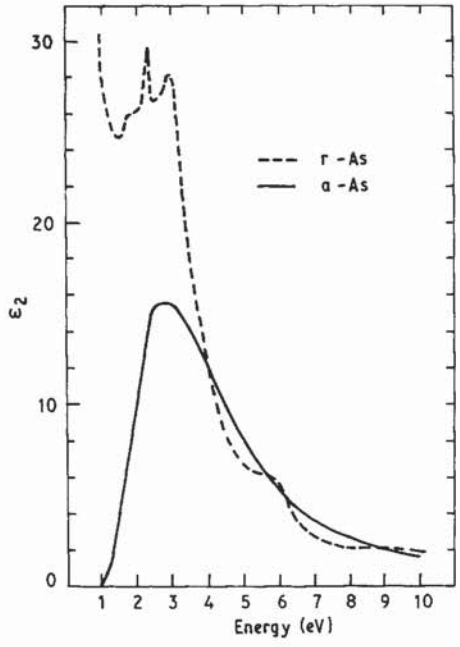

Comparison of the experimental ε_2 spectra of r-As and a-As, after [164, 38].

p-like σ and σ^* states. The calculations and XPS data find a small overlap between the s- and p-like valence bands near -6 eV [169]. The p bands is found to have three features in XPS and the s band is twin-peaked. Interestingly the s band of NaP_{15} (structurally related to Hittorf's phosphorus) also has a twin-peaked structure in spite of its content of five-fold rings [169]. Calculations of the s band [175] show that the Hittorf structure is a special case in which the ordered arrangement of five-fold rings can still produce a twin-peaked character, albeit somewhat asymmetric in shape. Amorphous (red) P also possesses a twin-peaked valence s band in XPS [169], indicating that a-P either has few odd-membered rings or that they are paired together as in the NaP_{15} structure and Hittorf's phosphorus. The p band of a-P is narrower indicating a loss of secondary bonding compared to o-P [169]. This also results in the optical gap of a-P being much wider than that of o-P [176].

A major difference between a-P and a-As is the increased importance of medium-ranged order in deposited a-P. A strong dependence on annealing is found in the rdf and Raman spectra of a-P, presumably due to a slow polymerization of P_4 units into a network [176, 177].

5.4. *a-S, a-Se and a-Te*

The chalcogens have an s^2p^4 valence configuration. Two of the p orbitals form σ bonds, leaving s and $p\pi$ lone pairs. The $p\pi$ lone pair states lie at the top of the valence band, giving chalcogens the alternative name of lone pair semiconductors [178].

The bonding of the crystalline phases can be viewed profitable from both the metallic and molecular limits. Te and Se possess trigonal phases (written here as t-Te and t-Se) consisting of spiral chains [179]. Se and S also crystallize in monoclinic (m-) phases with different stackings of Se_8 and S_8 rings. The chain structures are distortions of the simple cubic lattice of Po (see fig. 16), and revert towards this structure under pressure. The interchain distances (3·45 Å in Se and 3·50 Å in Te) are less than the van der Waals distance suggesting that important interchain bonding remains, of a resonant character [179, 180]. Under pressure the in-chain bonds remain almost constant in length while the inter-chain distances contract strongly. The ratio of intra- to interchain distances shows that interchain bonding is stronger in Te than Se.

Fig. 16

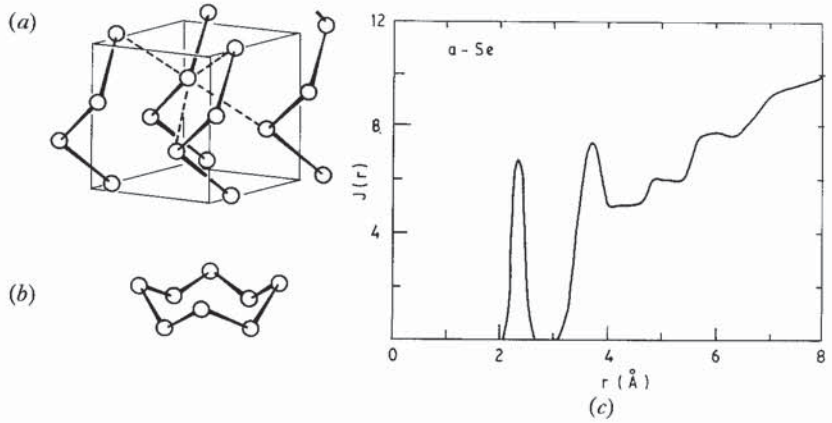

(*a*) Local order in trigonal Se and (*b*) Se_8 rings; (*c*) rdf of a-Se.

The rings and chains of m-Se and t-Se are notable for possessing both the same bond angle (103°) and the same dihedral angle, ϕ (101°). Their only difference is the manner in which the phase of ϕ varies (fig. 16): it alternates around a ring $+-+-$, but stays constant $++++$ or $----$ along a chain [181]. The π–π repulsion has introduced a rotational barrier around an Se-Se bond, constraining magnitude of ϕ to 101° in both structures [181], as in, for example, H_2O_2.

The SRO of a-Se cannot be deduced from the rdf alone [181–186] but only in combination with phonon [187–191] and photoemission spectra [192–196]. Assuming a bond angle $\theta \approx 103°$ in a-Se, as in m-Se or t-Se, the interchain distance and the magnitude and phase of ϕ must all be specified to define the SRO of a-Se completely, requiring the interpretation of atomic correlations out to 4·8 Å. A structural model [181] of a-Se as weakly interacting chains with locally ring-like dihedral-angle phasing has gained most acceptance [191, 185, 189]. It was originally deduced from photoemission data but its structural implications will be discussed first.

The weakness of the interchain bonding is apparent from the density deficit and rdf of a-Se. The second peak of the rdf centred on 3·75 Å contains six atoms, fig. 16(*c*) [181]. Two of these are intrachain and must lie near 3·69 Å for $\theta \approx 103°$. The remaining four are interchain and the rdf requires them to lie around 3·8 Å. This increased separation compared to t-Se (3·45 Å) or m-Se (>3·7 Å) is confirmed by a 12% density deficit compared to t-Se. Thus a-Se and a-As are similar in having weaker secondary bonding and density deficits.

The ratio of chain and ring-like configurations is deducible from the phonon spectra. The proportion of discrete Se_8 rings in a-Se is known to be small because of its low solubility in CS_2 in the dark [191]. To progress further, we first note that the dihedral angle is constrained in the chain-like structure of a-Se, unlike in a-Si or a-As. In the latter, highly co-ordinated networks the dihedral distribution arises as a by-product of ring closures. In contrast, a-Se has a low co-ordination and its network is underconstrained by its bond stretching and bending forces [40] so now ϕ can possess a sharp distribution, which we suggest is peaked at 101°, as in m-Se or t-Se.

The vibrational frequencies of ring (*cis*) and chain (*trans*) fragments are similar because of similarities of their angles and force constants, but the symmetries of such modes may vary [191]. The *cis* configuration possesses two A_1 modes at 113 and 256 cm^{-1} (fig. 17), the trans only 256 cm^{-1}. The 113 cm^{-1} mode can thus be used as

Fig. 17

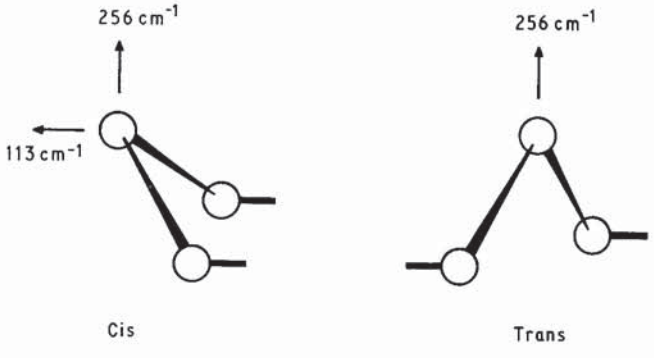

The A_1 vibrational modes of chain-like and ring-like fragments in a-Se.

a measure of the proportion of ring-like *cis* fragments in the chains of a-Se [191]. The sharpness and polarization of this 113 cm^{-1} line is evidence for a well-defined dihedral angle in a-Se; Se_6 with $\phi = 76°$ does not possess this mode [197].

The 256 cm^{-1} A_1 mode was originally used as evidence against chains in a-Se [187]. This mode lies at 256 cm^{-1} in m-Se but drops to 237 cm^{-1} in t-Se. The absence of lowering in a-Se was used to argue for Se_8 rings in a-Se. The lowering is now known to arise from interchain effects which increase in t-Te or in t-Se under pressure [179, 191] but are almost absent in m-Se or a-Se. Thus, this mode is degenerate in isolated rings and chains and cannot be used as a discriminant.

There are a number of reliable LDF pseudopotential and OPW calculations [198–205] which confirm the TB nature of states in Se and Te. The bands of t-Se (fig. 18) group into triplets in the trigonal polytypes, and the DOS groups in the same manner in all polytypes. The lowest valence band peak is *s*, followed by peaks due to $p\sigma$ and $p\pi$ states, as seen from explicit calculations of the charge density (fig. 19 (*b*)). The lowest conduction band is $p\sigma^*$, followed by a second gap and a second conduction band. This band has free electron-like character with s^*d states at its lower end. Charge density calculations show that the first conduction band states are truly $p\sigma^*$ and very localized, unlike the delocalized σ^* states of Si. TB parameters for Se and Te are derived by fitting the LDF bands, but using the experimental optical gaps (Se 1·85 eV, Te 0·34 eV) [206, 207].

Fig. 18

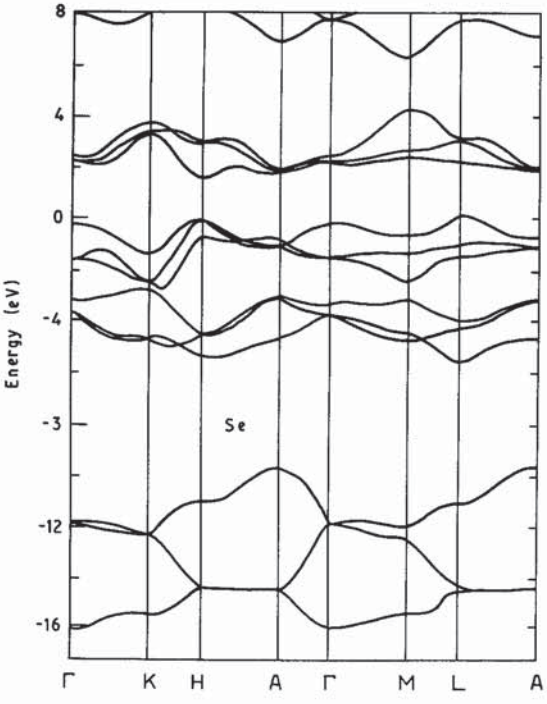

Calculated bands of t-Se (after [199]).

Fig. 19

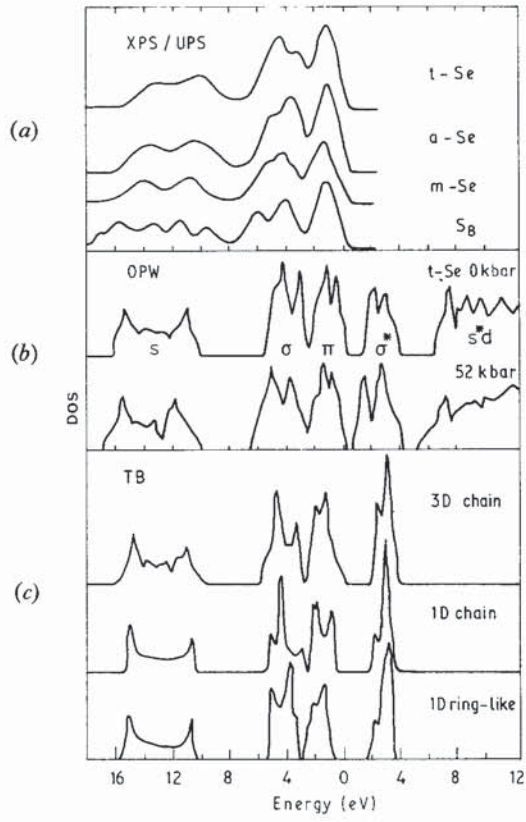

(*a*) Composite DOS of t-Se and a-Se [192], XPS of m-Se and S_8 [194]. (*b*) OPW DOS of t-Se at 0 kbar [203]. (*c*) Calculated TB DOS for chain- and ring-like structures using the parameters of table 1, for t-Se, isolated chains and isolated ring-like chains of Se.

Many aspects of the structure of a-Se and a-Te can be deduced from the different valence band DOS of t-Se and a-Se seen in photoemission [192] (fig. 19). The slight sharpening of the twin-peaked *s*-like lowest peak in a-Se is the reverse of the effect in a-Si and results from a reduction in interchain coupling [160]. The greatest difference is seen in the $p\sigma$ DOS which is a split peak from $-2{\cdot}5$ to -5 eV. The lower part of this peak is larger in t-Se while the upper part is larger in a-Se [192, 193]. This intensity reversal has been attributed to increased interchain distances, but without a calculation at the new distance [198]. It was also attributed to a lowering of the dihedral angle to 78° for Se_6 rings [208], but such angles are energetically unfavourable. The author [181] attributes the reversal to a preponderance of ring-like fragments in a-Se (fig. 19 (*c*)). This is confirmed by its similarity to the DOS of m-Se [184] and o-S [193] (fig. 19 (*a*) and (*c*)) and formed the basis of the model used earlier to interpret the phonon spectra.

The effect of the dihedral angle constraint is seen in evaporated a-Se. Highly disordered a-Se is produced by low-temperature evaporation. The lower $p\sigma$ peak in

the DOS is more intense in such films [195]. This is consistent with a structure in which the phase of ϕ is random [205]. The Raman spectrum [189] supports this interpretation without finding that a precise rotational barrier on ϕ exists.

a-S and a-Te have been studied in much less detail. S only polymerizes above its melting point at 430 K, and so bulk-quenched a-S contains discrete S_8 rings. Its valence band DOS is similar to a-Se [209–211]. The rdf of a-Te has been interpreted in terms of short chains [212]. Its phonon spectrum also shows evidence of independent rather than closely coupled chains [179, 213]. The photoemission data of Te and Se differ somewhat around 2–4 eV in the region of their σ states. The peak reversal in Se is not seen between t-Te and a-Te [192]. This may be due to the overlap of σ and π states found in band calculations [199], which is not present in Se.

The excitation spectrum of the Se 3*d* core level again gives data on the partial *p* DOS of the conduction bands [163, 192, 214]. The strong first peak is largely a core exciton and confirms the *p*-like character of the lower conduction band. The gap below the second conduction band seen in band calculations is confirmed by the strong dip in the experimental spectrum at 60 eV. A comparison of the spectra of a-Se and t-Se (fig. 20) confirms that the second conduction band starts at roughly the same energy in each case. Calculations [199, 203] indicate that this conduction band gap closes rapidly under pressure.

Disorder changes the optical spectra of chalcogenides and group IV semiconductors in characteristically different fashions [215]. The sharply peaked ε_2 spectrum of c-Si becomes a single broad, red-shifted peak of a-Si (fig. 8). The ε_2 spectrum of most chalcogenides consists of two peaks below 10 eV, both of which survive disordering (figs. 21 and 22). The lower and higher energy peaks are frequently attributed to $\pi \rightarrow \sigma^*$ and $\sigma \rightarrow \sigma^*$ transitions, respectively [216–220] (fig. 21 (*a*)). These assignments are based on TB ideas and unfortunately are not fully

Fig. 20

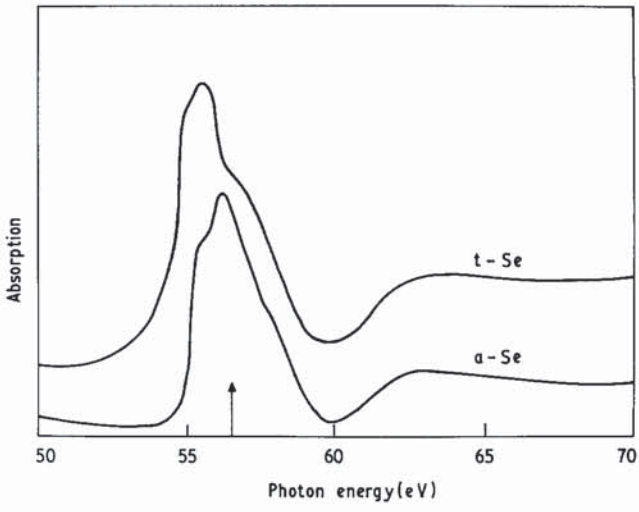

Core spectra of Se 3*d* level in c-Se and a-Se. The arrow indicates the onset of core-to-band transitions, as estimated from photoemission.

Fig. 21

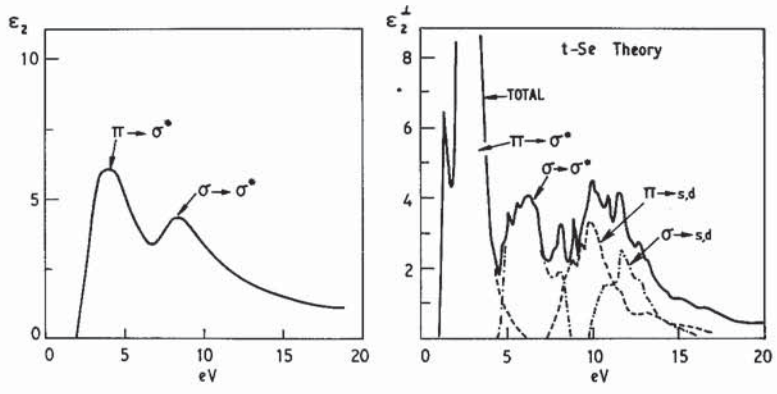

(*a*) Conventional interpretation of ε_2 spectra of a-Se. (*b*) The band-to-band decomposition of transitions in ε_2 of t-Se.

Fig. 22

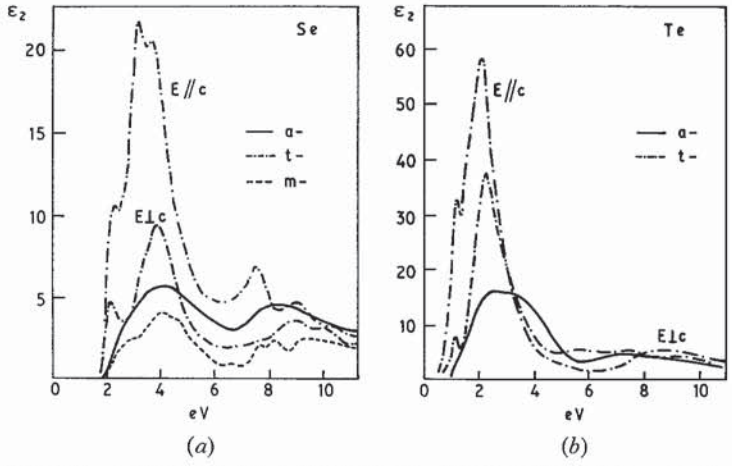

(*a*) Experimental ε_2 spectra of t-Se, a-Se and m-Se. (*b*) Experimental ε_2 spectra of t-Te and a-Te.

supported by more accurate calculations on t-Se and t-Te [200, 202, 203], as discussed shortly.

The ε_2 spectra of $\parallel$ and $\perp$ polarizations of t-Se [221, 222] (fig. 22) can be considered as two regions below and above 5·5 eV. The large peak at 4 eV must be due to $\pi \rightarrow \sigma^*$ transitions. Its intensity in a-Se is much less than that of the polarization-averaged ε_2 of t-Se but it has a similar size in m-Se [223]. We show that the optical coupling of π states to unoccupied states is much lower than that of σ states for geometric reasons. In terms of localized orbitals (fig. 23), the coupling of a bonding state is large [76]: $M_\sigma = \langle \sigma | x | \sigma^* \rangle$. However, the equivalent intramolecular term for π states to on-site σ^* states: $M_{\pi,1} = \langle \pi | x | \sigma^* \rangle = 0$, by symmetry. Thus, the

Fig. 23

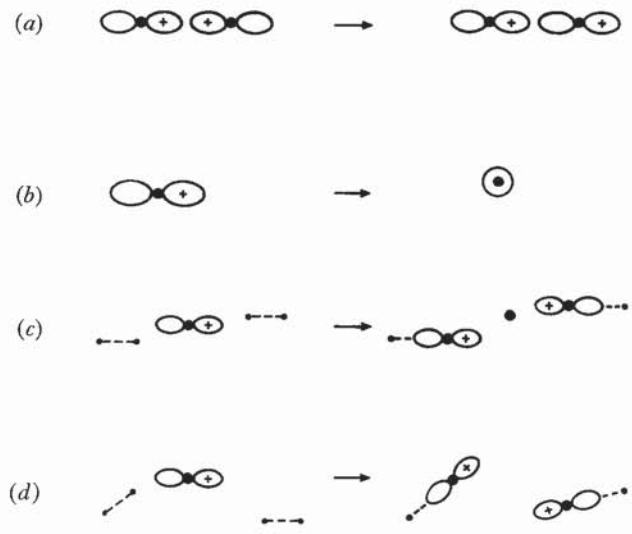

Illustrating the TB optical matrix element for: (*a*) $\sigma \rightarrow \sigma^*$ transitions; (*b*) $\pi \rightarrow s^*$ transitions; (*c*) $\pi \rightarrow \sigma^*$ interchain transitions in t-Se; and (*d*) $\pi \rightarrow \sigma^*$ transitions in a-Se.

only excitation to σ^* states originates from second-order terms, either to neighbouring σ^* states of the same chain, or by intermolecular terms $M_{\pi,2}$ to neighbouring chains such as shown in fig. 23 (*c*) and (*d*). The author interprets the smaller ε_2 peak at 4 eV in a-Se and m-Se as an indication that $M_{\pi,2}$ is smaller than in t-Se, due to a misalignment of π and intermolecular σ^* states in these phases. The corollary is that the oscillator strength of π states may not be exhausted by $\pi \rightarrow \sigma^*$ transitions, especially in a-Se, increasing the importance of transitions to the second conduction band. Such $\pi \rightarrow s^*d$ transitions commence at 8 eV in the theoretical spectra [200, 202] and involve only intra-atomic matrix elements like $\langle p|x|s^* \rangle$ (fig. 23 (*b*)). All transitions to the second conduction band are expected to be relatively independent of disorder because they involve only intra-atomic matrix elements and because core spectroscopy shows this band to start at the same energy in both t-Se and a-Se (fig. 20). If such transitions were important in a-Se, the oscillator strength of π electrons would not be exhausted until over 10 eV. An experimental spectrum for N_{eff} (effective number of electrons) would be valuable in this regard.

The second ε_2 peak is conventionally assigned to $\sigma \rightarrow \sigma^*$ transitions, but the author believes the alternative $\pi \rightarrow s^*d$ assignment could also be supported by comparing theoretical and experimental ε_2 spectra (fig. 21 (*b*)). Acknowledging that the LDF calculations [200, 202] underestimate the minimum gap, as usual, they place $\sigma \rightarrow \sigma^*$ transitions at 7 eV in Se where there is a dip in the more heavily weighted experimental $\varepsilon_2^{\perp}$. In contrast, the experimental $\varepsilon_2^{\perp}$ peaks at 8·5 eV where $\pi \rightarrow s^*d$ transitions dominate. Experimentally, N_{eff} is quoted to reach 4 electrons per atom (equivalent to the exhaustion of σ and π electrons) at 13 eV in t-Se [196], 11 eV above the π bands, so clearly $\pi \rightarrow s^*d$ are important in the overall ε_2 spectra.

The optical spectra of group IV and VI elements also behave in characteristically different fashion with applied pressure. The optical dielectric constant ε_0 decreases with pressure in c-Si, a-Si and other tetrahedrally bonded semiconductors, while it increases in t-Se and a-Se [216]. Also the optical absorption edge increases in energy in Si with pressure while it decreases in Se. In isotropic covalently bonded solids, pressure contracts the bonds and, by scaling (24), quickly increases the average optical gap, E_g. As ε_0 is given by

$$\varepsilon_0 = 1 + \frac{E_p^2}{E_g^2}$$

in terms of the plasma frequency E_p, ε_0 decreases [101]. In contrast, ε_0 decreases with pressure in closed-shell systems like molecular crystals and ionic solids. The ε_0 of molecular solids can be expressed as the sum of constant molecular polarizabilities, and the pressure dependence can be attributed to increasing local field effects in a Lorentz–Lorentz treatment. Thus, Kastner suggested that Se was also a closed-shell solid, consisting of non-interacting chain molecules [216]. However, we now know that pressure considerably changes the band dispersions and gaps and can explain the changes in ε_0 and the absorption edge without any local field corrections [204]. In spite of its low co-ordination, Se does not belong to the molecular limit and the wavefunctions of different chains have significant overlap. For phonons we assume that the intermolecular lattice interaction decreases between t-Se and a-Se because of unfavourable angular correlations, rather than by a large decrease in electronic overlap. Thus, the molecules in a-Se are electronically coupled but only weakly coupled vibrationally.

The different pressure dependence of ε_2 of Si and Se can now be attributed to the different changes in bond lengths. In Si, pressure reduces bond lengths isotropically, while in Se it is a fair approximation that pressure only decreases interchain distances, leaving intrachain distances constant. Thus, a model was developed for Se which assumed ε_2 to depend on $\pi \rightarrow \sigma^*$ and $\sigma \rightarrow \sigma^*$ transitions and in which pressure left the intrachain $\sigma \rightarrow \sigma^*$ gap constant but reduced the average $\pi \rightarrow \sigma^*$ gap [219, 220]. The model explains the strong correlation between the pressure coefficient of ε_0 and the bonding dimensionality. Following these excellent empirical correlations, useful theoretical support for this model might show the unimportance of transitions to higher conduction bands and the pressure insensitivity of interchain matrix elements such as that in fig. 23 (*c*).

5.5. *l-Se, l-Te and l-Se_xTe_{1-x} alloys*

The fluid phases of the chalcogens are unique because the interplay of covalent and metallic bonding can produce either a metal, a semiconductor or a diatomic gas, and can be varied by the composition, temperature or pressure [224, 225]. We restrict our discussion of the liquid to the low-temperature regime and concentrate on its co-ordination driven metal–nonmental transition (MNMT).

Neutron and X-ray diffraction measurements indicate that the co-ordination of liquid (l-)Se is about two and weakly temperature dependent [226–228], while that of l-Te increased rapidly with temperature from below three in the supercooled liquid [229–231]. As in a-Se, l-Se contains both ring- and chain-like fragments [191, 232]. The MNMT can be followed by conductivity, thermopower, Hall effect or NMR

Knight shift data [233, 234]. NMR suggests that the transition occurs by an increase in $N(\varepsilon_f)$ and that it is relatively gradual in l-Te, so that a diffusive transport regime exists for temperatures just above the melting point 450°C [234]. The changes in density of states, $N(\varepsilon)$, are driven by a change in co-ordination [235] which can be followed in the alloys by diffraction, density or sound velocity measurements [229, 236–238]. The chain-like phase is less dense, and a relatively sharp dip in density is observed against the steady fall with temperature due to normal thermal expansion. Increasing Se content is found to delay the onset of the MNMT and the co-ordination increase to higher temperatures and pressures [228, 229].

The suggested origin of the MNMT may be understood from schematic electronic DOSs constructed for various bonding configurations [224, 235]. The DOS of the disorder chain-like units in l-Se is similar to that of a-Se, with ε_f lying between the π and σ^* states (fig. 24 (*b*)). The overcoordinated structure of l-Te is frequently modelled by cross-connected chains. Tourand *et al.* [229] noted that the first and second co-ordination numbers n_1 and n_2 varied in the opposite sense but maintained $n_1 + n_2 = 6$. Thus, this structure of l-Te is derived from the simple cubic by a distortion with a variable number of short and long bonds with encompasses both the a-Se and a-As type structure [235]. Figure 24 (*c*) shows the DOS for a

Fig. 24

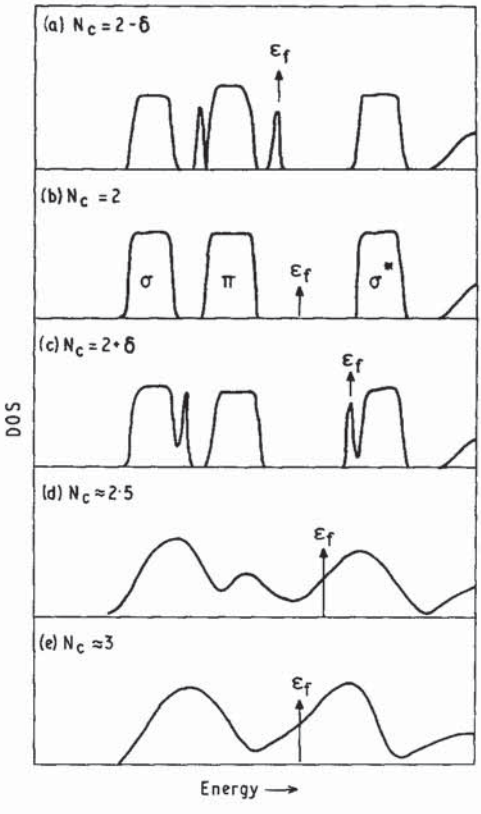

Schematic changes in DOS of l-Se.

network containing a small number of three-fold sites, fig. 24 (*d*) a large number of three-fold sites and fig. 24 (*e*) a network with all three-fold sites. Three fold sites convert π states into σ and σ^* states, as described in more detail in the defects section (§ 8). The DOS of fig. 24 (*e*) is related to that of As but ε_f lies well into the σ^* band because Te is p^4 rather than p^3. In contrast, broken chains convert σ and σ^* states into a second π state at the chain end and add states to the valence band maximum (fig. 24 (*a*)).

In this model, based on a TB view, these changes in the DOS of σ, π and σ^* states depend very generally on the SRO but this leads to a conflict with the thermopower data. For p^4 systems increasing the co-ordination above two places ε_f in a region of increasing DOS, or positive $\partial N(\varepsilon)/\partial\varepsilon$, while co-ordinations below two give $\partial N(\varepsilon_f)/\partial\varepsilon < 0$. Now, for diffusive transport, as in l-Te, the thermopower is given by:

$$S = \frac{e}{kt}\frac{\partial \ln N(\varepsilon)}{\partial \varepsilon}, \quad \text{at } \varepsilon = \varepsilon_f.$$

Experimentally, $S > 0$ in the diffusive regime of l-Se_xTe_{1-x} alloys [233] implying a negative slope, in direct conflict with that deduced above for a system with As-like SRO. There are a number of possible resolutions to this problem. The rdf of Tourand *et al.* [229] possesses a second-neighbour peak at 3·8 Å which is not present in the Fourier-enhanced data of Enderby and Gay [230]. This calls into question our proposition of an As-like structure. The second question is the relative stability of one- and threefold sites. The onefold and threefold sites (C_1^0 and C_3^0) are the co-ordination defects of chalcogens. In a-Se the singly occupied (neutral) defects are metastable with respect to the two charged states C_1^- and C_3^+ (§ 8). In Se-rich l-Se_xTe_{1-x} alloys, the paramagnetic neutral state C_1^0 is occupied by thermal excitation [239]. The C_1^0 and C_3^0 configurations are related by the formation of a dative covalent bond, which acts to delocalize the paramagnetic π electron into the σ^* states of C_3^0 sites. This delocalization would allow the relative stabilities of C_1^0 and C_3^0 to be studied by ESR. As the MNMT originates from such sites in the present model, such a study may throw light on the thermopower conflict. Finally, as the basic $\sigma - \sigma^*$ splitting and band gap is larger than in Se than in Te, the high pressure MNMT of l-Se is 'crisper' than that of l-Te and may allow a better separation of the factors involved, in spite of the greater experimental difficulties of handling the high pressures.

The interest in the liquid chalcogens arises because they maintain relatively low co-ordination numbers. In contrast, the co-ordination of other elemental liquids is sufficiently high to convert them into metals [240]. l-Si and l-Ge have co-ordinations of 6·4 and 6·8, respectively, similar to the disordered simple cubic structure or β-Sn. l-Sn and l-Pb are good metals with co-ordinations of 10·9, near the close-packed limit. The liquids are an important reference phase in the dielectric theory of bonding because of their lack of covalence [101]. It should be noted that although l-Sn and l-Pb are good metals, there is clear evidence in UPS of a separation of *s* and *p* states from a smooth free electron DOS along the series l-Ge to l-Pb and l-Al to l-Tl [241].

5.6. *a-B*

The conventional picture of bonding at a single B atom is of three sp^2 hybrids forming the familiar σ and σ^* states (fig. 3) with the unoccupied p_z π states forming

the lowest unoccupied levels. Such sites are found in boron's alloys. However, B itself also exhibits more unusual bonding configurations of higher co-ordinations involving three-centre bonding. The allotropic structures of c-B are classic examples of this situation [242]. There are few experimental studies of the structure of a-B [243, 244], but it appears that B atoms retain the remarkable icosahedral structures found in the various crystalline polytypes. Amorphous hydrogenated boron, a-B : H, is a p-type semiconductor with an approximately 1·5 eV gap [245]. This system also exhibits three-centre bonding, familiar from the chemistry of B hybrides. There are many features of the electronic structure of B sites in amorphous semiconductors which require further study.

§6. Short-range order and bonding in multicomponent systems

6.1. *The determination of short-range order*

Alloy studies are of potentially much greater interest in the non-crystalline state because alloys of more widely different elements can be formed. The bonding in any alloy must usually be deduced from a combination of thermochemical, structural and transport data. We first seek evidence of compound formation at compositions from extremes in the optical gap or resistivity or from anomalously small molecular volumes and large heats of formation [9–11]. This usually occurs at compositions satisfying chemical valences. For instance two metals may form charge-transfer semiconductors rather than simple alloys if their electronegativity difference is large. Four general classes of alloys are observed [246]:

(1) Two metals forming a series of metallic alloys, including those which order but remain metallic, such as Cu_3Au.
(2) Two semiconductors forming a series of covalent semiconductors, possibly with chemical ordering at some stoichiometric composition, but with the bonding following a CRN.
(3) Two metals with a tendency to form a charge-transfer semiconductor.
(4) A metal and a semiconductor form an alloy series, which usually possess a strongly ordered semiconducting compound. This is actually a combination of classes (2) and (3).

The structural distinction between categories (1–3) is the degree of chemical ordering, which is clearly the most important piece of experimental information we need to know.

We noted in §2.1 that the experimental determination of structure quickly becomes a daunting task as the number of constituents rises. The rdf is composed of partial rdfs which must all be specified. This requires three independent measurements for a binary system. We briefly review some of the favoured methods: neutron diffraction EXAFS and Raman spectroscopy.

The total structure factor S_t is the sum of the partial structure factors $S_{ij}(q)$ weighted by the composition and the atomic scattering factors, f_i. Three independent neutron diffraction measurements of S_t can be obtained by varying the individual f_i by isotropic enrichment. Although expensive this method has proved valuable data on many important liquids—NaCl, $NiTe_2$, Tl_2Te, CuCl, etc. [11, 230, 247]. In some fortunate situations $S_t(q)$ itself is sufficient. If the atomic radii of the two constituents A and B are very different, as in SiO_2, the AA, BA and AB

correlations occur at different distances in the total rdf. This allows the important parameters r_1, N_c and θ to be extracted [248]. The second noteworthy situation is when a small prepeak occurs in $S_t(q)$ at q_p, before the main peak (at q_m). This is evidence for ionic ordering [11, 249]. The characteristic of ionic ordering is that ions maximize their number of opposite neighbours and form screening shells [250, 251]. This causes both $S_{AA}(q)$ and $S_{BB}(q)$ to peak positively at q_p while $S_{AB}(q_p)$ is strongly negative. At the main peak all three terms are positive. Thus, the three correlations add a q_m to give the main peak but largely cancel at q_p, leaving the prepeak [249]. It should be noted that chemical ordering can result from a short-ranged preference for unlike neighbours as well as from ionic Coulombic forces [250]. Near-neighbour correlations do not distinguish these origins, this requires a study of the partial rdfs at large distances where S_{++} and S_{--} are forced into synchronism to screen the Coulombic forces [11]. Thus the prepeak indicates chemical ordering but not necessarily strong charge transfer.

EXAFS (extended X-ray absorption fine structure) is the small oscillations on core absorption edges due to the scattering of the outward-going electron wave by surrounding atoms. The absorption is related by a Fourier transform to the rdf about that site [21–23]. For a binary alloy, these two partial rdfs are often sufficient to allow the local structure to be deduced. In practice EXAFS data need very careful interpretation as the calculated bond lengths and co-ordination numbers depend very sensitively on the input atomic phase shifts. Calibration on similar crystals is generally recommended. As atomic phase shifts change monotonically with atomic number EXAFS is best able to detect chemical ordering in alloys of elements of different size.

Lattice vibration studies have been a valuable source of data of bonding, particularly in network solids [21, 252, 253]. In the absence of k-selection, Raman and infra-red spectra each reflect the total density of phonon states, but weighted by different matrix elements [254]. The phonon spectra of covalent networks can be accurately modelled by valence force-field descriptions, usually retaining only first-neighbour bond stretching and bond bending spring constants. The phonon DOS for any network with only nearest-neighbour force constants can be mapped into the electronic DOS of the equivalent TB hamiltonian [254–256].

Phonon DOS are interpreted by calculating the modes of model structures. Often, these need only be molecules AX_n with the same vertex SRO. Co-ordinations and ordering in As and Ge chalcogenide glasses have been studied by this means [252]. Clearly large mass differences between the constituents help to discriminate between the various possibilities. Many modes are Raman inactive in crystals, essentially due to the inversion symmetry of the homopolar covalent bond [254]. Such modes become active when the symmetry is lowered, by bond angle distortion in a-Si or because of the aysmmetric position of second neighbours as in trigonal Se [257]. Certain local configurations produced enhanced matrix elements and persist in the disorder phases, such as $(Si\text{-}O)_4$ rings in a-SiO_2 and boroxyl rings in a-B_2O_3 [258–260].

Finally, gross forms of chemical ordering can be detected by photoemission [261, 262]. The s bands DOS of crystals containing only AB bonds splits into two peaks due to s states on each atom. This splitting is a very general property of chemical ordering arising from the isotropy of s_σ interactions, and the splitting can even be used to define an ionicity scale [263]. Thus, the DOS of the valence s band seen by XPS is a very general probe of chemical ordering [262].

6.2. *Ionic ordering and the metal–nonmetal transition*

Composition-dependent metal–nonmetal transitions (MNMT) are a common feature of non-crystalline alloys of elements of significantly different electronegativities. Such differences cause a charge transfer from cation to anion and thereby an ionic chemical ordering [11, 246, 250]. The origins of the MNMT are most easily understood in the ionic limit [246, 264]. Recalling the TB description of ionic solids, the cation (C) states form the conduction band and anion (A) states the valence band. In this manner the composition x determines the number of conduction and valence states in the alloy C_xA_{1-x}. As both C and A are metals, ε_f lies near the band centres of the pure elements. Increasing the anion concentration from $x=1$ in fig. 25 (b) causes ε_f to drop within the C band, pass through the gap at stoichiometry, $x=0{\cdot}5$, and enter the band of A states. We call this the band-filling model of an MNMT.

The composition-dependence of the conductivity σ and thermopower S behave in a standard fashion for alloys (fig. 26) which obey the band-filling model [246] because of the behaviour of the localized states at each band edge [264]

Fig. 25

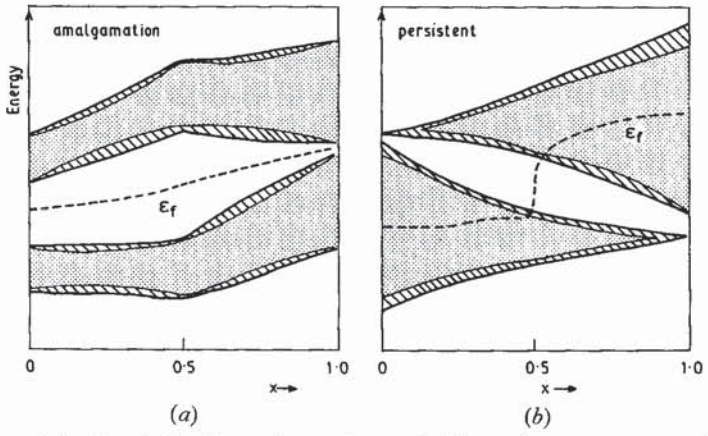

Development of the bands in (a) amalgamation and (b) persistent type amorphous alloys, showing localized states (shaded) and the movement of ε_f.

Fig. 26

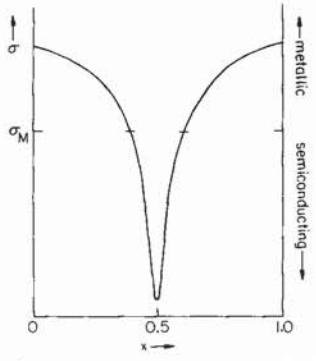

Schematic change in conductivity in persistent alloy obeying the band-filling model.

(fig. 25). According to Mott and Davis [1], states become localized when the DOS drops below about one-third of the free-electron DOS. Thus, the mobility edges lie at a definite distance into the bands, perhaps 10% of the overall bandwidth. Now, σ passes through the minimum metallic conductivity σ_m when ε_f passes through a mobility edge, so the alloys are semiconducting, with $\sigma < \sigma_m$ and $\partial\sigma/\partial T > 0$, for a specific range of compositions, perhaps $\pm 5\%$ about stoichiometry. Hence while the lowest conductivity depends on the size of the pseudogap, the width of the conductivity minimum, defined at σ_m, is independent of the system if the band-filling model holds. The movement of ε_f through the pseudogap can be visualized as the doping of the ionic compound M^+X^- by either M^+ ions, releasing electrons, or X^- ions releasing holes. This results in a sign reversal in the thermopower as the composition passes through $x = 0{\cdot}5$. This sign reversal can be used as a signature of the formation of ionic compounds [246].

So far for simplicity, we have only considered the MNMT in the fully ordered ionic limit, which we now relax, Alloy spectra (or bands) can be classified into two types, persistent and amalgamation [265]. In the persistent case, the alloy band structure resembles a weighted sum of those of the pure constituents, retaining many features of each element. In the amalgamation case, feature of the alloy bands evolve continuously with composition. Persistent spectra are found in the ionic limit, when the ratio of interatomic energy differences exceed the interatomic coupling by 0·5 [265]. In terms of the Weaire–Thorpe parameters, this is $V_3/V_2 \geqslant 0{\cdot}25$. Clearly, amalgamation spectra correspond to the covalent and metallic limits. We see immediately that systems displaying MNMTs belong to the persistent category, which establishes a purely electronic criterion for this behaviour. Chemical ordering enhances persistent behaviour by separating like atoms, thereby reducing the like-atom interactions and the widths of the cation and anion-like bands and increasing the effective size of V_2. Although apparently relegated to a subsidiary role in this definition, in real systems chemical ordering remains a pre-requisite for observable MNMTs. A number of workers have used Bethe lattice methods to study the dependence of the MNMTs on the degree of chemical ordering and ionicity [266–271]. As the ionicity falls, the well-defined gap becomes filled in, to leave a dip in the DOS. Ultimately, persistent behaviour expresses the situation that the dip in the DOS remains and that atoms add states to their own band, i.e. increasing anion concentration increases the size of the valence band, not both bands.

6.3. *Co-ordination, bonding type and ionicity scales*

Chemical ordering is expected in covalent as well as ionic alloys because heteropolar bonds are stronger [246]. Bonding in alloys can then be considered in two stages, at the ordered, stoichiometric composition(s) and away from stoichiometry. Co-ordinations vary in characteristically different ways from stoichiometry in covalent and ionic systems [246]. Covalent co-ordinations usually remain constant, following the 8-N rule, so excess of either constituent introduces like-atom bonds (fig. 27). In contrast ionic systems prefer to maintain unlike neighbours so co-ordinations must vary (fig. 28).

The type of bonding determines movements in ε_f and whether or not MNMTs occur. In some alloys, one type of bonding is found for all compositions, or sometimes it differs on each side of stoichiometry [11, 246]. Ionic co-ordinations away from stoichiometry give rise to MNMTs, as described in §6.2. On the other

Fig. 27

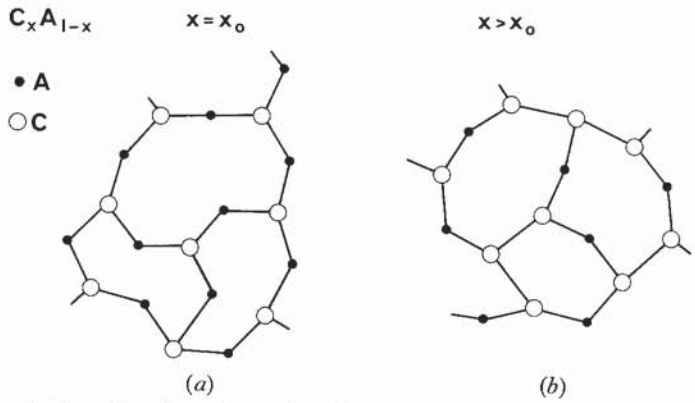

CRN of a chemically ordered covalent alloy C_xA_{1-x} [246]: (*a*) at stoichiometry, $x=0{\cdot}5$; and (*b*) at $x>0{\cdot}5$.

Fig. 28

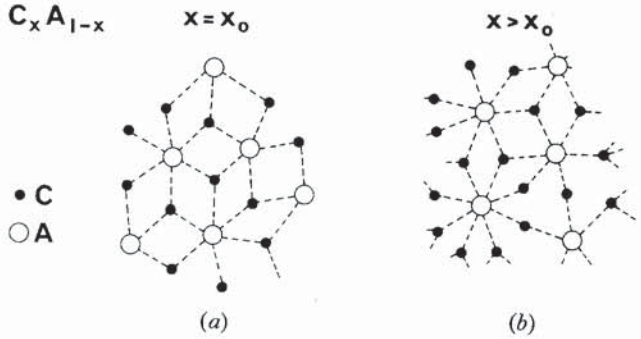

Structure of ionicially-ordered alloy C_xA_{1-x}: (*a*) at stoichiometry, $x=0{\cdot}5$; and (*b*) at $x>0{\cdot}5$.

hand, if the bonding is covalent and co-ordinations follow the 8-N rule, valence states are always occupied and ε_f remains in the gap. The strength of heteropolar bonds which encourages chemical ordering also causes $\sigma-\sigma^*$ splittings and optical gaps to peak at stoichiometry. The chalcogenide systems As_xS_{1-x}, and As_xSe_{1-x} and Ge_xTe_{1-x} follow the 8-N rule throughout their composition range. The variations in bands in such systems is shown schematically in fig. 25 (*a*) [272, 273].

Frequently, the bonding differs on either side of stoichiometry. Many interesting systems have only been studied as liquids, for which only resistivity, thermopower or Hall coefficients are most easily measured. The author has considered ways of deducing the bonding type from variations in such transport properties [246].

Ionicity is expected to be the main factor determining bonding type in non-crystalline alloys, as it is in crystals. Mooser and Pearson [274] were the first to realize that crystal structures could be classified using two rather than one variables, and were able to analyse the structure of many AB, AB_2 and AB_3 compounds. They used the difference in Pauling [78] electronegativity and the principal quantum number. Phillips and Van Vechten [275–277] restricted their attention to the 8-electron crystals and used a dielectrically-defined ionicity to distinguish the zincblende and wurzite

compounds from ionic compounds with the NaCl and CsCl structure. Most recently, a very effective classification of the crystal structure of over 100 AB compounds was achieved using r_σ/r_π parameters [278–280], derived from non-local atomic pseudopotentials [281, 282]. Many other phenomena such as chemical shifts of core levels, NMR and vibration frequencies depend on ionicity. Thus, there is great demand for semiempirical, but quantitative methods of describing bonding. We review the more common methods to calculate ionicities, so the user may make the choice.

Pauling [78] defined electronegativity as the electron attracting ability of atoms. Several compilations exist [283], but this method is now considered inadequate in not distinguishing the effects of s and p electrons or different co-ordinations.

Sanderson [284] introduced an ionicity scale based on very simple ideas of atomic screening which has been used to systematize vibrational frequencies in a-Si : H [253].

Charge densities from TB band calculations give ionicities. The first general discussions of TB ionicities used the context of the BOM [77] (§ 3.3). Ionicity values are by-products of many calculations reported here. When comparing TB ionicities, it is important to ensure that the approximations and assumptions remain constant.

The dielectric theory [275–277] perhaps provides the most general recipe to find ionicity. The theory was constructed for 8-electron compounds like GaAs. The ionicity f_i is defined in terms of the homopolar gap E_h and the ionic gap C:

$$f_i = C^2/(E_h^2 + C^2). \tag{27}$$

E_h is taken to depend only on bond length d (Å) as:

$$E_h = 39{\cdot}74\, d^{-2{\cdot}48}\ \text{eV}. \tag{28}$$

Levine [285] generalized these formulae to apply to any crystal and they can be further generalized to apply to any SRO in terms of the co-ordinations. Each system is decomposed into its constituent two-centre bonds. (These bonds are not necessarily the 2-electron covalent bonds.) The number of electrons associated with each bond, N_e, is determined by apportioning valence charge:

$$N_e = \frac{Z^a}{N_c^a} + \frac{Z^b}{N_c^b}, \tag{29}$$

where Z^a is the valence charge and N_c^a is the co-ordination of site a. The electron density must now be found from the product of N_e and the number of these bonds per Å^3 (N_b). Levine found an empirical relationship between N_b and the average co-ordination number of the bond, N_c, of a compound A_mB_n:

$$\overline{N}_c = \frac{m}{m+n} N_c^a + \frac{n}{m+n} N_c^b, \tag{30}$$

$$\nu = 0{\cdot}095 \overline{N}_c (\overline{N}_c - 1) \tag{31}$$

and

$$N_b = \nu d^{-3}, \tag{32}$$

where ν is the normalized number of bonds per unit volume.

The screening exponent in C is found for distances (in Å) from:

$$k_s r = 2{\cdot}729 (N_e \nu)^{1/2} r^{1/2} \tag{33}$$

giving finally the ionic gap C as

$$C = 14{\cdot}4b\left\{\frac{Z_a}{r_a} - \frac{Z_b}{r_b}\right\}\exp(-k_s r), \tag{34}$$

where r_a and r_b are the radii of sites a and b. The prefactor b is an empirical constant which Levine found to obey:

$$b = 0{\cdot}089\overline{N}_c^2. \tag{35}$$

The ionicity of any system can be found by this prescription by decomposition into bonds. The optical dielectric constant ε_0 can also be found using E_h, C and the plasma frequency calculated from N_e and N_b.

Although many formal objections could be raised against the Levine method, its advantages are that (*i*) its only input is co-ordinations, valence and atomic radii, (*ii*) it can handle a wide variety of bonding situations giving ionicities in accord with experience.

Finally, we discuss the remarkable ionicities which can be extracted from non-local quantum-defect pseudopotentials [278–280]. The core potential has a hard core and is expressed as a sum of Coulombic and quasicentrifugal terms:

$$V = -\frac{Z}{r} + \sum_{\hat{l}} \frac{\hat{l}(\hat{l}+1),}{r^2}, \tag{36}$$

where $\hat{l}$ are non-integer parameters playing the role of the angular momenta, l, which are fitted to atomic spectra or calculated pseudopotentials. Characteristic radii for the s and p valence orbitals, r_s and r_p, are defined by:

$$r_s = \frac{\hat{l}_s}{Z}, \quad \text{etc.} \tag{37}$$

The r_σ, r_π parameters are found by taking linear combinations for sites a and b:

$$r_\sigma^a = r_s^a + r_p^a, \qquad r_\pi^a = r_p^a - r_s^a \tag{38}$$

and then

$$r_\sigma = r_\sigma^a - r_\sigma^b, \qquad r_\pi = r_\pi^a + r_\pi^b. \tag{39}$$

Strong correlations were found between $r_\pi^{-1} \propto E_h$ and $r_\sigma \propto C$. Thus, r_π^{-1} plays the role of the covalent gap and r_σ the role of ionic gap [279], and ionicities could be found using the proportionality constants.

The quantum defect parameters provide remarkable structural classifications of AB compounds. Compounds with 10 electrons per formula unit (e.g. GeTe) are p bonded and r_σ is defined as a p-electron ionicity [286]:

$$r_\sigma^a = r_p. \tag{40}$$

It is suggested that a similar redefinition for the s-bonded 2-electron compounds (e.g. CsAu) is used [246]:

$$r_\sigma^a = r_s. \tag{41}$$

However, the method has yet to be generalized to A_mB_n compounds and is not yet a fully tested route to empirical ionicities, comparable to that of Levine.

§ 7. Electronic structure of specific binary systems

7.1. *Arsenic chalcogenides*

The amorphous chalcogenides are amongst the simplest and most highly studied alloys. As_2S_3 and As_2Se_3 crystallize in a layer structure in which As is threefold and S/Se is twofold bonded, in accord with the 8-N rule. In contrast, c-As_2Te_3 has complex structures with threefold Te sites and a mixture of sixfold and fourfold As sites [287]. These co-ordinations clearly do not satisfy the 8-N rule and are evidence of resonant covalence or partial metallic bonding. The rdfs of bulk glassy As_2S_3 and As_2Se_3 indicate that chemical ordering and 3 : 2 co-ordinations are retained [288]. The rdf and As-edge EXAFS of glassy As_2Te_3 show the presence of 3 : 2 co-ordinations, unlike in c-As_2Te_3 [289].

The valence configurations of As (s^2p^3) and the chalcogen (s^2p^4) are used to form p-like σ orbitals, deep s-like non-bonding states and a chalcogen $p\pi$ lone pair. In photoemission [290] (fig. 29) the As and Se s states lie below -7 eV and the π peak at -2 eV merges into the σ peak at -4 eV. The spectra of crystal and glass for each compound are similar, as expected for As_2S_3 and As_2Se_3. This was not expected for As_2Te_3 because of the co-ordination change. However, the weakly bonded Te p states of c-As_2Te_3 lie at the same energy as the Te π states of a-As_2Te_3 [290].

Band calculations [291] of single layers of As_2S_3 and As_2Se_3 confirm this simple bonding picture, but find a gap between π and σ states. A three-dimensional band calculation of c-As_2Se_3 using EHT found this gap to be washed out and found a strong $\sigma-\pi$ mixing due to interlayer interactions [292]. However, we believe EHT tends to overestimate distant interactions, as discussed in § 2.2, and that the upper valence band consists largely of Se π states.

Fig. 29

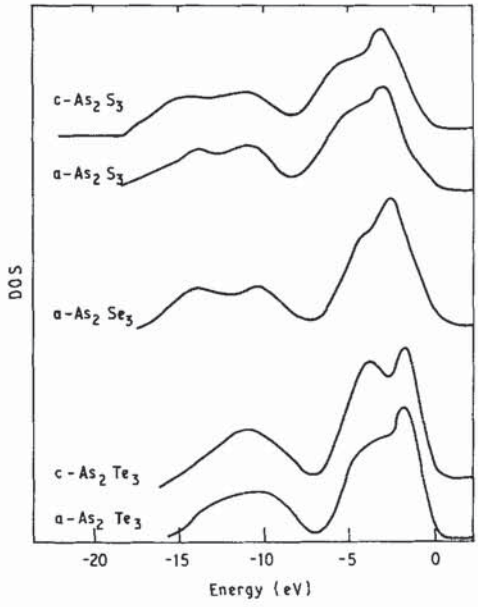

Combined UPS/XPS DOS of (*a*) c- and a-As_2S_3, (*b*) c- and a-As_2Se_3 and (*c*) ci and a-As_2Te_3.

The As–S and As–Se bonds are weakly polar. Raman, EXAFS and core spectra give evidence for almost complete chemical ordering in a-As_xS_{1-x} and a-As_xSe_{1-x} at $x=0{\cdot}4$ [252, 293–295]. EXAFS finds 93% ordering in annealed a-As_2S_3 [293]. As x moves away from stoichiometry like atom bonds are introduced but the co-ordinations remain 3 : 2. Arsenic telluride glasses are more complex, their rdfs and NMR show evidence of threefold Te sites in Te-rich glasses [287, 296].

Chemical ordering is strongly dependent on annealing in a-As_2Se_3. As–As bonds in As_4Se_4 units are seen in freshly evaporated films by EXAFS [293], and they have a notable effect on the valence DOS [297].

The prepeak in the diffraction pattern of a-As_2Se_3 [288] is also dependent on annealing. This peak is usually associated with layer-like intemediate-range order [288], such as the formation of 'outrigger rafts' [295]. Note, however, more general clustering, rather than simple layer-like ordering, has also been suggested as responsible for the prepeak in such systems [298]. This argument is based on the observation that l-Na possesses such a prepeak and certainly does not contain layers.

7.2. *Germanium chalcogenides*

The simplest structural model of a-Ge_xX_{1-x} (X = chalcogen) is a random network of fourfold Ge and twofold X sites in which the number of Ge – X bonds is maximized, giving an ordered composition at $x=0{\cdot}67$ [252]. There is increasing evidence that deviations from this model exist, both in the degree of ordering at $x=0{\cdot}67$ and in the retention of only 4 : 2 co-ordinations. There is evidence of subsidiary chemical ordering at $x=0{\cdot}5$ in a-GeS and a-GeSe associated with 3 : 3 co-ordinations.

The calculated electronic structure of c-$GeSe_2$ (fig. 30 (*a*)) serves as a good basis for that of chemical ordered a-GeX_2 [299]. The electron configuration of Ge s^2p^2 and Se s^2p^4 produces four σ states per Ge site, and non-bonding s and π Se states. The Se s states lie at -14 eV, the σ states from -2 to -8 eV and the π states from 0 to -2 eV. The lowest conduction band is unusually narrow and consists of σ^* Ge s/Se p states. The narrowness of the band arises from the small interaction of two σ^* states at each

Fig. 30

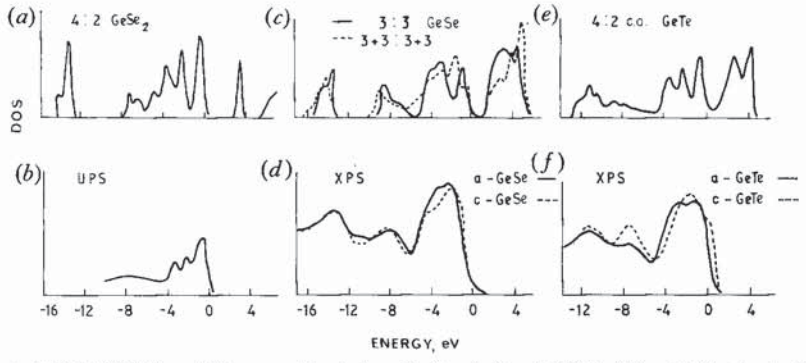

Calculated TB DOS for: (*a*) co-ordinated c-$GeSe_2$ (after [299]); (*b*) c-GeSe including only intralayer interactions (3 : 3) or including also interlayer interactions (3 + 3 : 3 + 3) after [107]; (*c*) 4 : 2 co-ordinated, chemically-ordered GeTe (after [261]); (*d*) UPS data of a-GeS_2; (*e*) XPS data of c-GeSe and as-deposited a-GeSe (after [312]); and (*f*) XPS data of c-GeTe and a-GeTe (after [313]).

Se site due to its near 90° bond angle (a similar decoupling at the Se vertex is found in lattice vibrations [256]). The Ge p states form higher σ^* states.

Strong chemical ordering is evident in a-GeS_2 and a-$GeSe_2$ from their Raman spectra [252, 293]. Nemanich *et al.* [293] estimated that fewer than 7% of homopolar bonds were present in annealed a-$GeSe_2$. A 235 cm^{-1} post-peak in the Raman spectrum of a-$GeSe_2$ has been attributed to Se–Se bonds [300], but the interpretation is incomplete. The Mossbauer spectra of transmitting ^{129}Te impurities provides stronger evidence for incomplete chemical ordering in a-$GeSe_2$ and a-GeS_2 [301]. The Se–Se bonds produce localized σ^* gap states [299].

The addition of excess Ge or chalcogen can be followed in the Raman spectra as the introduction of Se_3Ge–$GeSe_3$ or Se–Se units [252, 293, 302], within a 4 : 2 co-ordinated network. However, there is the possibility of a subsidiary ordering at $x = 0{\cdot}5$, with 3 : 3 co-ordinations. X-ray and neutron diffraction data, EXAFS, infrared and Raman spectra often lead to conflicting interpretations [303–311]. Recently, we have some confidence that the structures of a-GeS, a-GeSe and a-GeTe can best be distinguished from their valence s band DOS seen in XPS [261, 262, 312–314]. Chemically ordered a-GeSe is only possible for a 3 : 3 structure because a 4 : 2 structure inevitably contains Ge–Ge bonds. Such bonds broaden the Ge s peak at −8 eV (fig. 30 (*b*)). The most recent experimental XPS DOS show that a-GeSe is 3 : 3 co-ordinated and a-GeTe is 3 : 3 if deposited at low temperatures but anneals towards a 4 : 2 structure [314].

The reduced back-bonding causes changes in the DOS of 3 : 3 a-GeSe from that of c-GeSe, fig. 30 (*b*). As in a-As (fig. 13), the optical gap is opened up. The top valence band also starts to split off from the lower p bands. Hence the valence DOS develops an upper peak resembling that of Se π states in a-$GeSe_2$. Thus, an upper valence peak is not an infallible indication that chalcogens are twofold co-ordinated.

This discussion of the details of the co-ordinations of a-GeSe and a-GeTe should not distract attention from the fact that 4 : 2 co-ordinations hold for the majority of a-Ge_xSe_{1-x} alloys and all annealed a-Ge_xTe_{1-x} alloys, in accord with the 8-N rule, but in contrast to c-GeSe and c-GeTe. This is another manifestation of the greater importance of intramolecular bonding compared to resonant or secondary bonding in amorphous phases [180]. Resonant bonding requires longer-ranged atomic correlations than the simple covalent pair bond [180, 315], but produces only a small gain in cohesive energy, so it is less favoured in amorphous semiconductors. In the elements As and Se the loss of resonant bonding merely results in an increase in back-bonded distances. In c-GeSe resonant bonding stabilizes formal charges of Ge^+Se^- which allows trivalent bonding. The resonant bonding collapses in most a-IV–VI alloys, causing a return of 8-N co-ordinations. The retention of 3 : 3 bonding in a-GeSe but not a-GeTe may be related to their different structures of c-GeSe and c-GeTe [261]. In the orthorhombic structure of c-GeSe, two of the four back-bonds are intralayer, while c-GeTe is rhombohedral and all of its back-bonds are interlayer. Thus, if a-GeSe can maintain orthorhombic-like intralayer correlations, then some resonant bonding can remain to stabilize its 3 : 3 co-ordination. The dihedral angle is a measure of orthorhombic to rhombohedral ordering and appears to favour the *cis* configuration for lighter elements such as a-GeSe and a-P.

As in a-As_2Se_3 chemical ordering and co-ordination are strongly dependent on annealing. In a-$GeSe_2$ annealing greatly decreases the fraction of homopolar bonds, and the bonding changes are visible in UPS [293, 313]. Bonding changes can also be induced by light—photostructural changes—which are particularly strong in the

germanium chalcogenides [316–319]. These changes are excited by photons of energy just less than the band-gap. Many mechanisms have been suggested—defects [317], bond-angle changes [316], processes involving bistable bonding configurations [316] or heteropolar bonds, but no consensus has been reached. The changes are accompanied by a parallel shift of the optical absorption edge to lower energies (photodarkening). As photodarkening has been observed in a-Se [318] it cannot be due to a photo-induced destruction of heteropolar bonds. Recent diffraction studies find that the structure factor is modified out to the largest wave numbers, suggesting that bond length changes must be involved [319].

The TB parameters for the 4 : 2 co-ordinated chalcogenides follow those of the elements. For the 3 : 3 co-ordinated forms, parameters can be scaled from those of As for use with free atom orbital energies, as described in §§ 4.2 and 5.4.

7.3. SiO_2

Amorphous SiO_2 has a 4 : 2 co-ordinated network, formally related to that of a-$GeSe_2$. However, the large 9 eV gap and 140° bond angle produce considerable differences in their electronic behaviour. The original CRN was developed for a-SiO_2 [36]. The bond length, bond angles and angle distortions can be extracted from the rdf because the various peaks do not overlap [248]. The strong similarity of the photoemission spectra, optical properties and defects of c- and a-SiO_2 is one of the remarkable features of SiO_2 which allows us to use crystalline analogues in the calculations with more confidence than in a-Si or a-As. The electronic structure of SiO_2 taxes many calculational methods because of its low co-ordination, low symmetry and low screening [320–330]. The TB DOS of α-quartz in fig. 31 displays many of the features of more complex calculations, and is similar to the XPS and UPS data [331–333]. The TB calculation uses an sp^3 basis on

Fig. 31

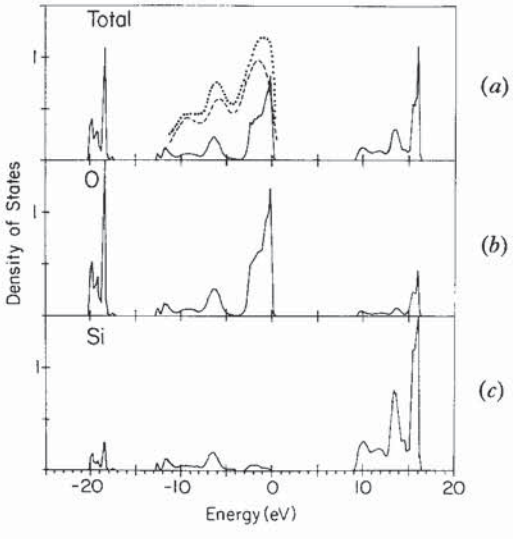

(*a*) TB DOS and XPS of SiO_2, (*b*, *c*) partial O and Si DOS.